Chemical Science

ROYAL SOCIETY OF CHEMISTRY

EDGE ARTICLE

View Article Online
View Journal | View Issue

Cite this: *Chem. Sci.*, 2025, **16**, 6918

All publication charges for this article have been paid for by the Royal Society of Chemistry

Received 15th January 2025
Accepted 11th March 2025

DOI: 10.1039/d5sc00364d

rsc.li/chemical-science

Anion-endowed high-dielectric water-deficient interface towards ultrastable Zn metal batteries†

Xiangjie Liu,[a] Xiaoxin Nie,[a] Yujiao Yang,[a] Meng Yao,[*b] Jiaxian Zheng,[c] Hanfeng Liang,[*c] Mi Zhou,[d] Jin Zhao,[e] Yingqian Chen[f] and Du Yuan[*a]

To achieve reversible metallic Zn anodes for aqueous rechargeable zinc batteries, regulating the electrolyte–Zn interface is the key to addressing the side reactions on Zn. Beyond water-deficiency, design rules for constructing the highly efficient electrochemical interface are still vague. Anions, as primary electrolyte constituents, not only play a role in solvation structure, but also influence the electrolyte–Zn interface. Here, the characteristics of representative anions in current aqueous zinc electrolytes are surveyed. A candidate combining polarizability, H-bond tuning ability and high solubility is proposed to construct a high-dielectric water-deficient electrolyte–Zn interface to regulate the interfacial chemistry on Zn. The anion-dominated electrochemical interface promotes the Zn deposition kinetics and achieves uniform Zn deposition with high stability, which further enables the *in situ* formation of an SEI for highly stable Zn stripping/plating, *e.g.*, at 20 mA cm^{-2} and 20 mA h cm^{-2}. Furthermore, this built-in interface exhibits an effect in stabilizing the V_2O_5 cathode, endowing the V_2O_5/Zn cell with ultra-stable long-term cycling, *e.g.*, 10 000 cycles at 10 A g^{-1} with a high retention rate of 89.7%. Our design offers insight into guidelines for the development of novel electrolytes towards rationally designed electrochemical interfaces.

Introduction

Aqueous rechargeable batteries are attracting attention as next-generation energy storage alternatives. Benefitting from their metallic Zn anode, zinc metal batteries (ZMBs) have the merits of natural abundance, promising electrochemical performance, and environmental friendliness.[1–3] However, uncontrolled detrimental water-induced side reactions lead to deterioration in the lifespan of the Zn anode.[4–7] Water molecules can be reduced on Zn, where the hydrogen evolution reaction (HER) leads to an increase in local pH. This causes the uncontrollable formation of surface by-products, and the resulting uneven surface aggravates the nonuniform distribution of the electric field, accelerating dendrite growth and the HER. The above entangled factors significantly reduce the Zn utilization efficiency. To regulate the interfacial reactions on Zn anodes, a water-deficient inner Helmholtz plane (IHP) in an electric double layer (EDL) is typically proposed, which depresses water activity by altering the hydrogen bond (H-bond) characteristics *via* zinc salt concentration, additive, gelation, *etc.*;[8–23] however, these approaches have been insufficient to achieve the stable high utilization of Zn.

In the emerging zinc salts for ZMBs,[24–29] organic anions play an indispensable role in reshaping solvation structure from the conventional $[Zn(H_2O)_6]^{2+}$ configuration and H-bond network, based on their metal chelating characteristics and hydrophilicity/hydrophobicity. Unlike the solvent-dominant EDL in conventional nonaqueous electrolytes, anions can present strong affinity to the metal surface, causing water solvent molecules to be repelled. Hence, it is imperative to provide a comprehensive insight into the contributions of anions to constructing IHPs *via* the tuning of zincophilic interactions and H-bond characteristics. Additionally, the dielectric constant (*i.e.*, relative permittivity) represents the response of a material to an external electric field, where the regulated migration of charged species generates a collective electric dipole moment. The importance of dielectric properties is being underscored for rechargeable batteries,[30] *e.g.*, dielectric

[a]College of Materials Science and Engineering, Changsha University of Science and Technology, 960, 2nd Section, Wanjiali RD (S), Changsha, Hunan, 410004, China. E-mail: aduyuandu@outlook.com; yuandu@csust.edu.cn

[b]College of Materials Science and Engineering, Sichuan University, Chengdu, Sichuan, 610065, China. E-mail: yaomeng@scu.edu.cn

[c]State Key Laboratory of Physical Chemistry of Solid Surfaces, College of Chemistry and Chemical Engineering, Xiamen University, Xiamen 361005, China. E-mail: hfliang@xmu.edu.cn

[d]Ningbo Merak Advanced Materials Technology Co., Ltd, Lane 189, Canghai Road, Ningbo High-tech Zone, Zhejiang 315100, China

[e]State Key Laboratory of Organic Electronics and Information Displays & Institute of Advanced Materials (IAM), Nanjing University of Posts & Telecommunications, 9 Wenyuan Road, Nanjing 210023, China

[f]Department of Chemistry, National University of Singapore, Block S8, 3 Science Drive 3, Singapore 117543, Singapore

† Electronic supplementary information (ESI) available. See DOI: https://doi.org/10.1039/d5sc00364d

solvent protocols to manipulate interphase characteristics in liquid state electrolytes,[31,32] lithium salt dissociation in solid state polymer electrolytes,[33] and built-in field promoted ion transport in 3D gradient hosts.[34] In addition to influencing the solvation structure, the dielectric properties inherent to the molecular species in electrolytes could fine-tune the EDL region *via* intermolecular fields, facilitate charge transfer, diminish the ion concentration gradient and circumvent ion depletion to suppress dendrite growth. However, the impact of the dielectric contribution from anions has rarely been explored in aqueous electrolytes. Further, the formation of an *in situ* solid-electrolyte interface (SEI) is a feasible approach to address the deterioration of the interphase due to water-induced reactions; the constituents of the EDL and their electrochemical stabilities determine the SEI characteristics. Among the current novel approaches towards the formation of *in situ* SEIs on Zn, such as electrolyte additives,[35,36] aqueous/non-aqueous hybrid solvents,[29] and water-in-salt electrolytes,[37] the ability to form anion-derived SEIs is highly attractive for constructing stable electrolyte–Zn interfaces,[38] where the relatively positive reduction potential of Zn^0 (−0.76 V *vs.* SHE) compared with that of Li^0 makes the decomposition of anions in the electrolyte system become contentious.[39–41] Hence, the effects of anion-dominant IHPs on interfacial reactions on Zn warrants scrutinization.

Herein, the characteristics of representative anions in aqueous zinc electrolytes are first surveyed. Based on the correlated intrinsic properties, anions combining polarizability, H-bond tuning ability and aqueous solubility for the construction of a high-dielectric water-deficient electrolyte–Zn interface are proposed (Fig. 1a). We then demonstrate the tuning of the EDL, which impacts the interfacial chemistry on Zn, *via* a saturated fluorine-free hydrophilic eco-friendly anion without the use of additives or nonaqueous co-solvents. The anion-dominated high-dielectric interface can effectively repel water molecules and favor the desolvation process as verified by MD, thus promoting Zn deposition kinetics and achieving uniform Zn deposition. It further enables the *in situ* formation of an SEI for highly stable Zn stripping/plating, *e.g.* at 20 mA cm^{-2} and 20 mA h cm^{-2}. Further, the V_2O_5/Zn ZMB cell exhibits ultra-stable long-term cycling, *e.g.*, 10 000 cycles at 10 A g^{-1} with a high retention rate of 89.7%, and the role of the electrochemical interface in stabilizing the V_2O_5 cathode is revealed. We further demonstrate the extension of the high-dielectric interface *via* a gel electrolyte with the same type of anion.

Results and discussion

Correlation among the intrinsic properties of anions in aqueous zinc electrolytes

Via the Clausius–Mossotti relation, the macroscopic dielectric constant (ε_r) is correlated with microscopic polarizability (α).[42] To explore the contribution of anions to the dielectric properties, an investigation of the molecular polarizabilities of representative anions was first conducted using density functional theory (DFT) (Fig. 1b); their molecular polarizabilities followed the order PS^- (phenolsulfonate) > OTf^- (trifluorosulfonate) > SA^- (sulfamate) > SO_4^{2-} (sulfate) > OAc^- (acetate). The ESP values of anions represent their electronegativities,[43] and the

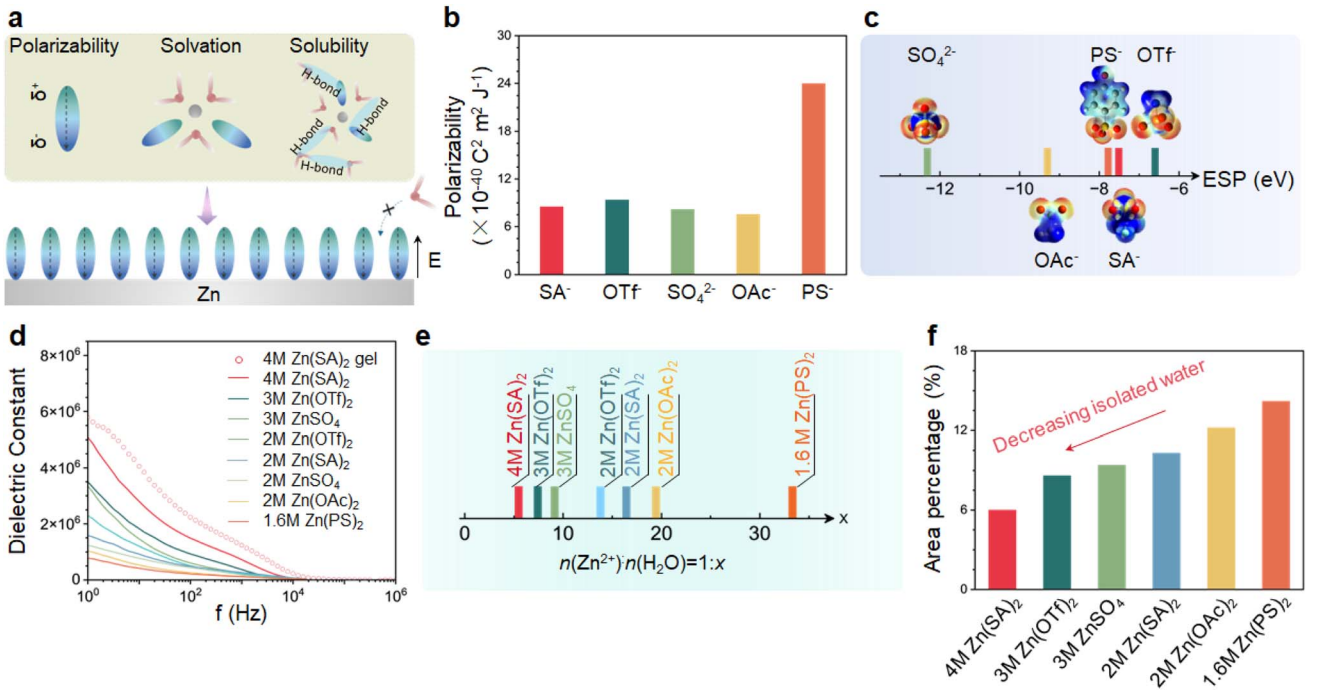

Fig. 1 Key factors for the construction of a high-dielectric water-deficient electrochemical interface. (a) Critical factors of anions for electrolyte–Zn interfaces. (b) Polarizabilities of anions in zinc salts. (c) ESP values of anions. (d) Dielectric constants of representative aqueous zinc electrolytes. (e) Solubilities of zinc salts expressed as the molar ratio of $n(Zn^{2+}) : n(H_2O) = 1 : x$. (f) Relative proportions of isolated water in aqueous zinc electrolytes.

calculated ESP values followed the order OTf^- > SA^- > PS^- > OAc^- > SO_4^{2-} (Fig. 1c). A more negative electrostatic potential (ESP) value indicates stronger interaction between opposite charges, suggesting high rigidity of the charge distribution and consequently low α. Except for PS^-, the decreasing α values with anions show increasing ESP values. The largest ESP value of SO_4^{2-} can be attributed to its divalent nature, and the discrepancy for PS^- might be ascribed to the delocalization of electrons on the benzene ring.

The dielectric properties of the corresponding aqueous zinc electrolytes for ZMB were then measured (Fig. 1d) at standardized molar concentrations and at their saturation concentrations. Among the saturated electrolytes, 4 M $Zn(SA)_2$ presents the highest dielectric constant; the dielectric constants of the saturated zinc electrolytes follow the order 4 M $Zn(SA)_2$ > 3 M $Zn(OTf)_2$ > 3 M $ZnSO_4$ > 2 M $Zn(OAc)_2$ > 1.6 M $Zn(PS)_2$. Note that the trend of the measured dielectric constants of the aqueous zinc electrolytes does not follow that of their anion polarizabilities exactly. Additionally, for a given zinc salt, increasing concentration leads to an enhanced dielectric constant. The above suggests that the dielectric contribution from the solvent, *i.e.*, water molecules, cannot be overlooked. Thus, the aqueous solubilities of the zinc salts were considered. To dissolve an ionic solid, its lattice energy must be overcome by the solvent. A large ε_r value for an anion favors the dissociation of the metallic cation and anion and leads to strong ion–dipolar interactions with solvent molecules, promoting salt dissolution. However, this intuitive model is a simplified one, since the solubility of a salt is complex, involving hydrophobicity, ion-pair interactions, deep eutectic interactions, *etc.* As a result, the empirical saturation concentrations of the zinc salts were determined (Fig. 1e) and expressed explicitly as the molar ratios of zinc ions to water molecules. Among the candidates, $Zn(SA)_2$ presents the highest solubility, *i.e.*, the molar ratio of $n(Zn^{2+}) : n(H_2O)$ of 1 : 5.5, which could be ascribed to the large ε_r and H-bond donor/acceptor characteristics of SA^-. The solubility trend of the aqueous zinc electrolytes coincides with that of their dielectric constants. This implies that anions with high polarizability and solubility are desirable in order to endow the electrolyte with promising dielectric properties.

Further, the ability of anion to alter the water states as well as the H-bond network was evaluated by deconvoluting the –OH stretching in the Fourier-transform infrared (FTIR) spectra of the zinc electrolytes (Fig. 1f and S1†). Three types of water states can be differentiated,[44,45] namely, weakly bonded isolated water (~3550 cm^{-1}), cluster water with an ice-like liquid state (~3400 cm^{-1}), and bulk water with an ice-like state (~3240 cm^{-1}); the relative proportion of free water was chosen to reflect the change in the water state. Among the candidates, 4 M $Zn(SA)_2$ significantly reduced the relative proportion of free water to ~6.0%. The ability of the anions to alter water state was further tested by fixing the molar ratios of the anion (SA^-, OTf^-, OAc^-, SO_4^{2-}) relative to the water molecules (Fig. S2†), and the promising ability of SA^- was associated with it having both an H-bond acceptor and donor.

Based on the intercorrelated characteristics/intrinsic properties of the anions, the fluorine-free and eco-friendly anion SA^- was selected to demonstrate the impact of a high-dielectric water-deficient electrolyte–Zn interface on regulating the interfacial chemistry.

Physicochemical properties of $Zn(SA)_2$ electrolytes

The inherited vibrational characteristics of the aqueous $Zn(SA)_2$ electrolytes from the corresponding zinc salt can be clearly observed in Fig. 2a (Fig. S3 and Table S1†), *i.e.*, deformation of $-NH_2$ at 1557 cm^{-1}, symmetric and asymmetric stretching vibrations of $-SO_3^-$ at 1245 and 1048 cm^{-1}, and $-SO_3^-$ deformation at 562 cm^{-1}. Additionally, the concentration-dependent tuning of the water states in the $Zn(SA)_2$ electrolytes shows that isolated and cluster water transform to bulk water as the electrolyte approaches saturation (Fig. S4†), *i.e.*, the relative percentage of bulk water increases from 80.6% to 87.5%, while those of isolated and cluster water drop from 10.3% to 6.0% and 9.1% to 6.5%, respectively (Fig. 2b and c), which indicates the effective adjustment of water activity and reshaping of the H-bond network. The changes in H-bond induced by $Zn(SA)_2$ were then verified *via* the deshielding effect as revealed in the ^1H NMR spectra; the significant broadening was attributed to complex interactions surrounding the H_2O molecules (Fig. S5†). To explore the solvation structure of Zn^{2+} in $Zn(SA)_2$ electrolytes, molecular dynamics (MD) simulations of the radial distribution functions (RDF) and coordination number (CN) distribution functions were conducted. The relatively shorter Zn–O length for O in SA^- (~1.8 Å) than that for water molecules (~1.9 Å) indicates the incorporation of SA^- into the zinc solvation sheath (Fig. 2d). As the salt concentration increases, CN_{SA^-} drastically increases from 0.8 (2 M) to 1.6 (4 M), indicating the significant replacement of water molecules in the first solvation sheath with CN_{H_2O} decreasing from 4.7 to 3.5. DFT calculations revealed the much stronger binding energy of Zn^{2+}–SA (−18.36 eV) compared to that of Zn^{2+}–H_2O (−4.73 eV) (Fig. 2e), indicating that Zn^{2+} prefers to bind with SA^- rather than H_2O. ESP mapping further confirmed the affinity of $-SO_3^-$ to Zn^{2+}, with the NH_3^+ group being exposed outwards (Fig. 2e). Thus, the MD snapshots in Fig. 2f display the solvation structure of 4 M $Zn(SA)_2$ (see also Fig. S6†), where Zn^{2+} is coordinated with three H_2O molecules and two SA^- in 4 M $Zn(SA)_2$.

The physicochemical properties of $Zn(SA)_2$ electrolytes were studied. The decreased water activity with increasing $Zn(SA)_2$ concentration leads to a higher onset potential of the oxygen evolution reaction, increasing from 2.26 V to 2.67 V *vs.* Zn/Zn^{2+} for 4 M $Zn(SA)_2$ with depressed current density compared to its counterpart (Fig. 2g), thus widening the electrochemical window from 2.32 V to 2.72 V *vs.* Zn/Zn^{2+} for 4 M $Zn(SA)_2$. Note that the lower intensity of the redox peak could be attributed to slower ion transport as discussed below. Additionally, better anti-corrosion properties can be obtained by tuning the $Zn(SA)_2$ concentration, with a positive shift of the corrosion voltage (from −0.94 V to −0.89 V *vs.* Ag/AgCl) and lower corrosion current density (from 5.90 to 5.28 mA cm^{-2}) being observed with increasing the concentration to saturation (Fig. 2h). The ion transport behavior of the $Zn(SA)_2$ electrolytes was also studied. The ion conductivity of the $Zn(SA)_2$ electrolytes

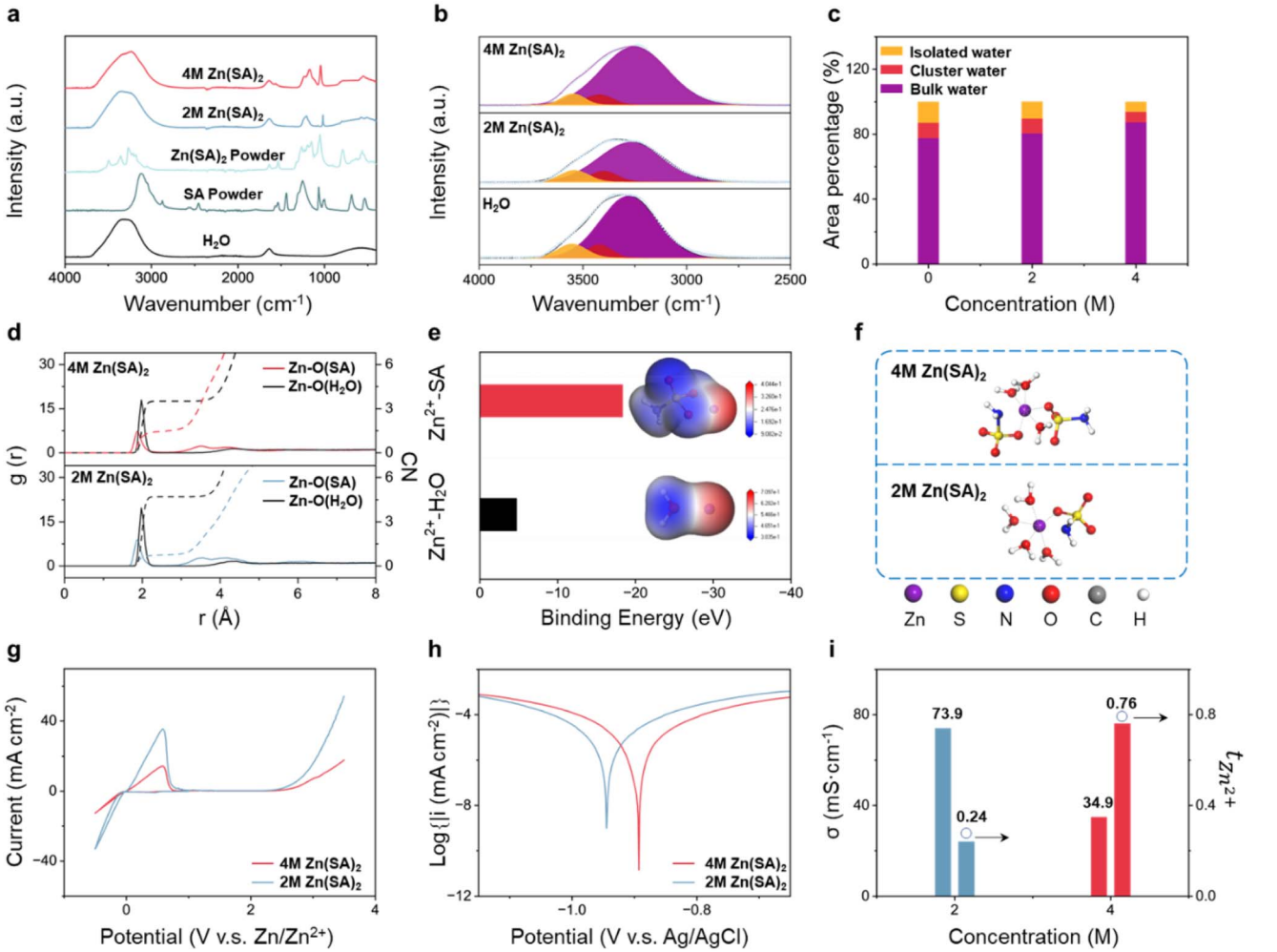

Fig. 2 Physicochemical properties of $Zn(SA)_2$ aqueous electrolytes. (a) FTIR spectra of $Zn(SA)_2$ electrolytes, and (b) deconvolution for −OH to compare the different water states and (c) their relative percentages. (d) RDF $g(r)$ and coordination number $CN(r)$ of Zn^{2+}–O_{H_2O} and Zn^{2+}–O_{SA} comparing 4 M and 2 M $Zn(SA)_2$. (e) Binding energies of Zn^{2+}–SA and Zn^{2+}–H_2O, with the ESP distribution of Zn^{2+}–SA and Zn^{2+}–H_2O. (f) MD snapshots comparing the solvation structures of 4 M and 2 M $Zn(SA)_2$. (g) Cyclic voltammetry curves of $Zn(SA)_2$ electrolytes at a scan rate of 1 mV s^{-1}. (h) Tafel plots comparing $Zn(SA)_2$ electrolytes. (i) Ion conductivities and transference numbers comparing different $Zn(SA)_2$ electrolytes.

decreases from 73.92 to 34.85 mS cm^{-1} with increasing concentration, which could be related to its large solvation structure (Fig. 2i). The transference number ($t_{Zn^{2+}}$) was also measured to understand the contribution of the cations to ion transport (Fig. 2i and S7†). The significant enhancement of $t_{Zn^{2+}}$ from 0.24 (2 M) to 0.76 (4 M) suggests the hindrance of anion motion, which could be ascribed to the greater incorporation of anions in the solvation sheath in 4 M $Zn(SA)_2$.

Zn deposition behavior on the $Zn(SA)_2$–Zn interface

The impact of the $Zn(SA)_2$–Zn interface on the Zn deposition behavior was then investigated. Coulombic efficiency (CE) was first evaluated by assembling Cu|Zn asymmetric cells under a constant current/capacity density of 1 mA cm^{-2} and 1 mA h cm^{-2}. During cycling, the Cu|Zn cell with 4 M $Zn(SA)_2$ exhibits a high CE of 99.9% from the first cycle, with the overpotential stabilizing from 76 mV (1st cycle) to 68 mV (10th cycle), 62 mV (50th cycle), and gradually to 60 mV (100th cycle) (Fig. 3a). In contrast, the cell with 2 M $Zn(SA)_2$ presents fluctuating polarization after ~82 cycles (Fig. S8†).

Using chronopotentiometry, the nucleation overpotentials for the Cu|Zn cells with 4 M and 2 M $Zn(SA)_2$ cells were determined to be 56.4 mV and 65.9 mV (Fig. 3b), respectively. The lower nucleation overpotential of the cell with 4 M $Zn(SA)_2$ indicates its favorable nucleation kinetics, leading to more uniform Zn deposition. The deposition behaviors for the $Zn(SA)_2$ electrolytes were further studied using chronoamperometry (CA) under a constant overpotential of −150 mV (Fig. 3c), which can sensitively reflect the changes in the active surface area during nucleation.[46,47] The cell with 4 M $Zn(SA)_2$ shows quick stabilization of the current density at ~472 s compared to ~1500 s for its 2 M counterpart, indicating a switch from a 2D mode (lateral nucleation/growth) to a 3D mode (vertical deposition). The fast switch to the 3D mode implies the saturation of the exposed surface area for Zn

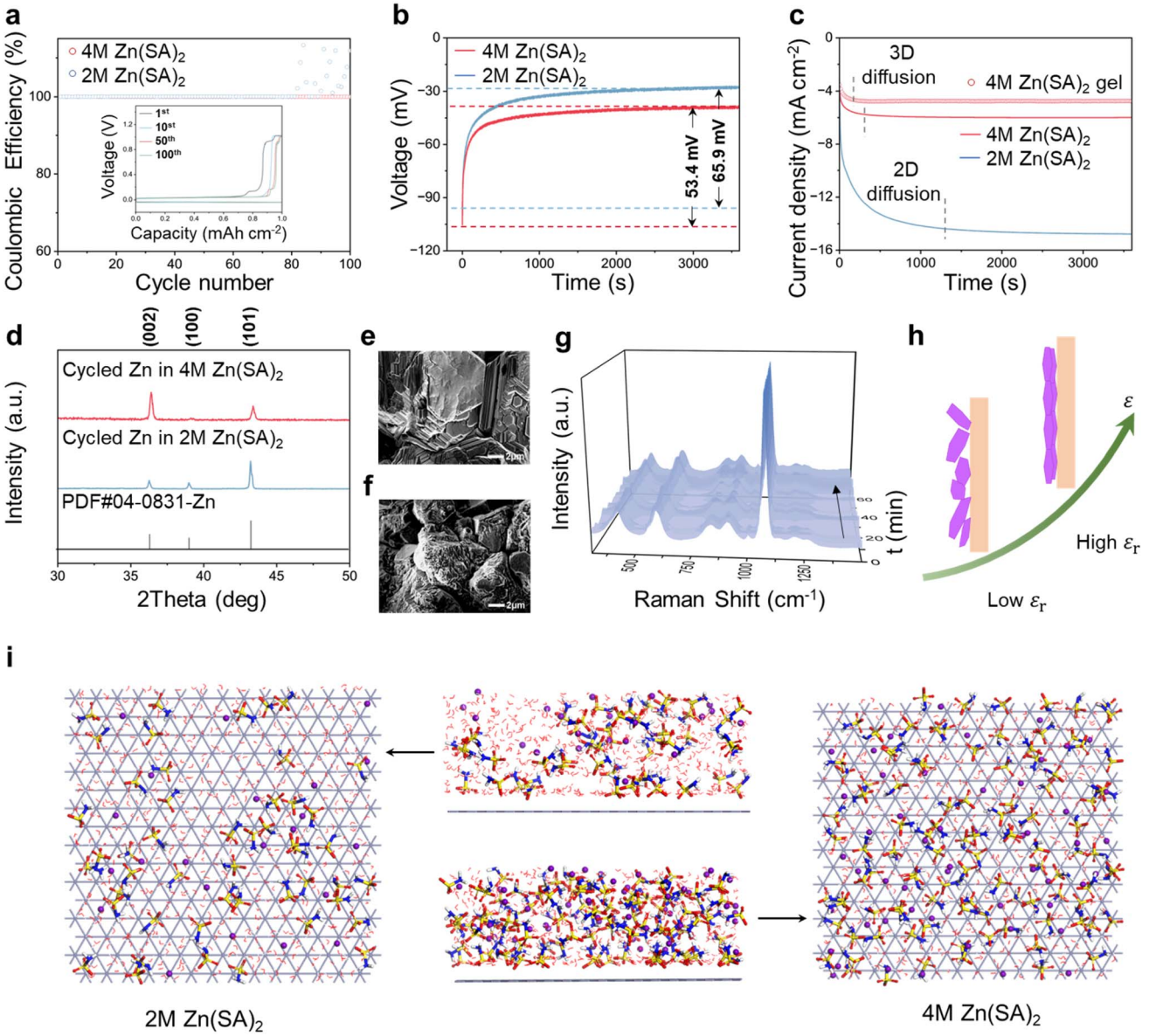

Fig. 3 Tuning Zn deposition behavior *via* a high-dielectric interface. (a) CEs of $Zn(SA)_2$ electrolyte in Cu|Zn cells, where the inset presents the corresponding polarization curves. (b) Nucleation overpotentials of Zn deposition for 4 M and 2 M $Zn(SA)_2$ electrolytes. (c) CA curves of Cu|Zn cells in $Zn(SA)_2$ electrolytes under an overpotential of −150 mV. (d) XRD spectra comparing the electrodeposited Zn for 4 M and 2 M $Zn(SA)_2$ electrolytes at 10 mA cm^{-2}, and corresponding SEM images comparing the morphology of the deposited Zn for (e) 4 M and (f) 2 M $Zn(SA)_2$. (g) Contour map for the time-dependent study of the deposition surface *via in situ* Raman spectroscopy. (h) Schematic diagram showing the influence of the dielectric constant on Zn deposition. (i) Electrolyte–Zn interface simulation. Ion and water molecule distribution at the interface for 2 M and 4 M $Zn(SA)_2$.

deposition, suggesting that 4 M $Zn(SA)_2$ is more conducive to uniform Zn deposition. Scharifker–Hills analysis[48] indicates that the CA of the 4 M $Zn(SA)_2$ electrolyte closely approaches the curve predicted by the instantaneous nucleation theory (Fig. S9†). X-ray diffraction (XRD) spectra was performed for Zn electroplated on Cu (Fig. 3d). At an applied current/capacity density of 10 mA cm^{-2} and 10 mA h cm^{-2}, the intensity ratio of (002)/(101) is 2.02 for the deposited Zn using 4 M $Zn(SA)_2$, which is much higher than that of only 0.28 obtained using 2 M $Zn(SA)_2$. Clearly, using 4 M $Zn(SA)_2$ is more conducive to exposure of the Zn(002) crystal plane (see also Fig. S10† for Zn deposition at 1 mA cm^{-2} and 1 mA h cm^{-2}). The exposure of the Zn(002) crystal planes using 4 M $Zn(SA)_2$ can be clearly verified by SEM (Fig. 3e and S11†), in contrast to the diversely oriented crystal planes obtained using its 2 M counterpart with a much rougher surface morphology (Fig. 3f). Additionally, the promotion of uniform Zn (002) deposition is exemplified at 1 mA cm^{-2} and 1 mA h cm^{-2} (Fig. S12†).

The regulated deposition behavior reflects the importance of a high-dielectric interface. *In situ* Raman spectroscopy was then applied to monitor the vibrational species on the interface. Compared to the spectrum of the bulk electrolyte, the

significantly blue-shifted O–S–O, degenerate $-SO_3^-$ deformation, and symmetric $-SO_3^-$ stretching at the electrolyte–Zn interface suggest the reshaping of the EDL by SA^- (Fig. S13†). These interfacial vibrational features were well retained during Zn deposition (Fig. 3g), reflecting the stabilization of the EDL, which will be further explored. MD simulation was applied to visualize the anion-dominated interface for 4 M $Zn(SA)_2$, in which water molecules are largely repelled from the interface (Fig. 3i and S14†). Accordingly, the merits of high-dielectric electrolyte–Zn have been depicted in Fig. 3h. The anion-induced high dielectric interface can effectively reshape the IHP, which presents a tendency to retain anion species.[49] The reshaped IHP can regulate the interfacial electric field and homogenize ion flux,[50] favoring interfacial ion transport and desolvation kinetics. This leads to an accelerated switch to the vertical growth mode and promotes uniform deposition with a Zn (002) texture, which can significantly suppress the growth of Zn dendrites,[51–56] in contrast to the nonuniform and disoriented deposits obtained using its low dielectric counterpart.

Electrochemical performance of the $Zn(SA)_2$–Zn interface

The rate performance of Zn stripping/plating in Zn|Zn symmetric cells was evaluated under a series of current densities from 0.1 to 20 mA cm^{-2} (Fig. 4a). The long-term cycling stability of the Zn|Zn cells using $Zn(SA)_2$ electrolytes was compared at 10 mA cm^{-2} and 10 mA h cm^{-2} (Fig. 4b and S15†). The polarization of the symmetric cell cycled in 4 M $Zn(SA)_2$ remained nearly constant (~143.8 mV at 10th cycle) after 2000 h (~112.2 mV), demonstrating its promising lifespan (see also Fig. S16† for comparison of 1 mA cm^{-2} and 1 mA h cm^{-2}). The cell with 4 M $Zn(SA)_2$ presents steady polarization even under a high current/capacity density of 20 mA cm^{-2} and 20 mA h cm^{-2} (DOD of ~34%) (Fig. S17†), in contrast to the rapid shorting with 2 M $Zn(SA)_2$; the symmetric cell with 2 M $Zn(SA)_2$ shorts after only ~100 h. In electrochemical impedance spectroscopy (EIS), the cell with 4 M $Zn(SA)_2$ shows a lower charge transfer resistance (R_{CT}) of 7.6 Ω than its 2 M $Zn(SA)_2$ counterpart (17.7 Ω) before cycling (Fig. 4c, S18 and Table S2†). The situation is maintained after cycling, with a lower R_{CT} (37.7 Ω) for 4 M $Zn(SA)_2$ than its 2 M counterpart (56.4 Ω). This indicates the beneficial interfacial charge transfer by 4 M $Zn(SA)_2$, favoring the reaction kinetics. This is further supported by the favored desolvation process in 4 M $Zn(SA)_2$ during each dehydration step (Fig. S19†). Additionally, EIS analysis suggests the possible presence of an SEI on Zn after cycling in $Zn(SA)_2$ electrolytes (R_{SEI} of 13.9 Ω, Fig. S18†). After cycling in 4 M $Zn(SA)_2$, the Zn anode is uniformly covered by a dark surface layer (Fig. 4d). An *ex situ* SEM study reveals that this surface

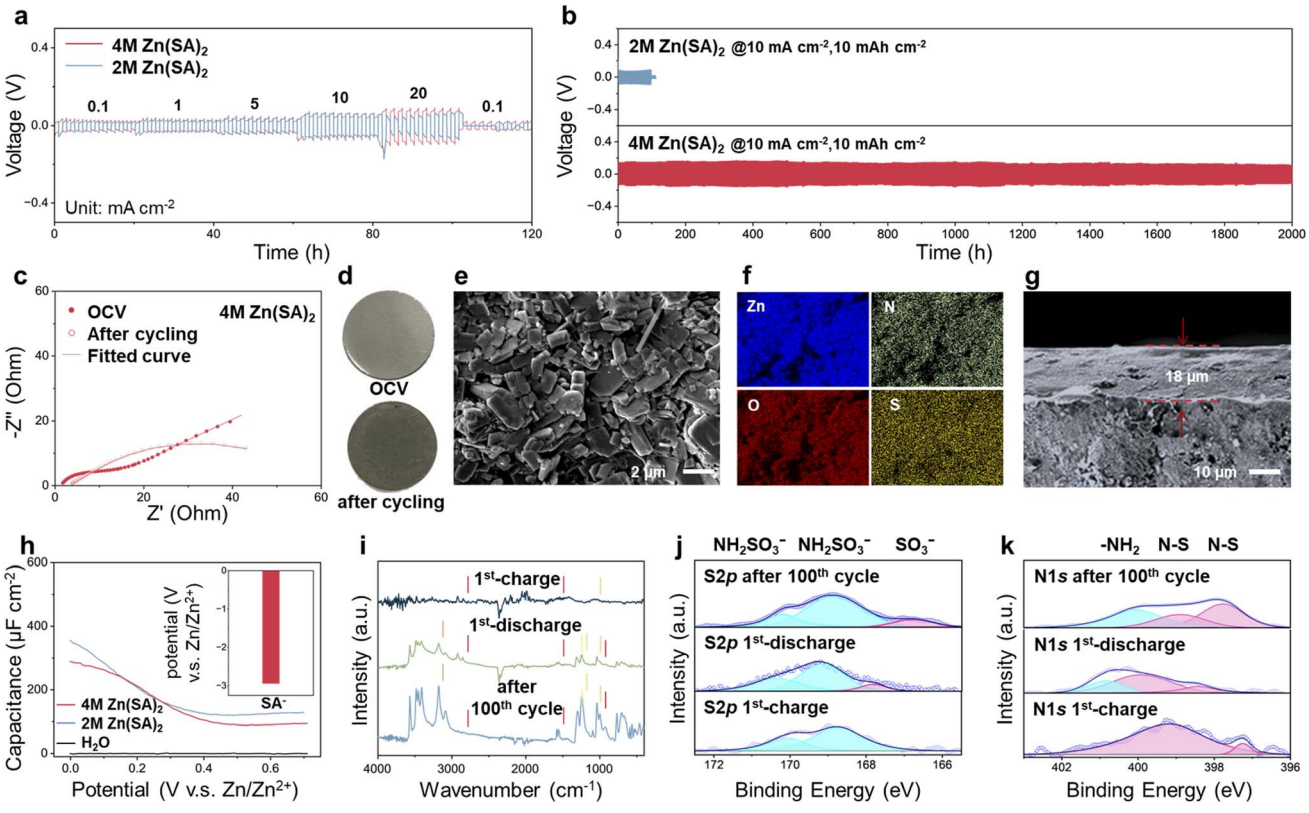

Fig. 4 Performance and characterization of the $Zn(SA)_2$–Zn interface. (a) Rate performance comparison of 4 M and 2 M $Zn(SA)_2$. (b) Zn plating/stripping at 10 mA cm^{-2} and 10 mA h cm^{-2}. (c) EIS spectra of the Zn|Zn cell with 4 M $Zn(SA)_2$ before and after 100 cycles. *Ex situ* characterization of the cycled Zn in $Zn(SA)_2$ electrolytes: (d) optical images of the Zn anode before and after cycling, (e) top-view SEM images with (f) EDX mapping indicating the presence of Zn, N, O, and S, and (g) cross-sectional view confirming the formation of a surface layer. (h) Non-faradaic capacitance–potential curves for the $Zn(SA)_2$ electrolytes. The inset shows the reduction potential of SA^- on Zn. Time-dependent (i) FTIR-ATR spectra and XPS analyses of (j) S 2p and (k) N 1s on the cycled surface.

layer consists of ~2–5 μm plate-like structures (Fig. 4e) with a uniform distribution of N, O, S, and Zn observed through EDX mapping (Fig. 4f), and is ~18 μm thick (Fig. 4g).

To analyze the electrochemical interface, alternating current voltammetry was applied to determine the concentration-dependence of the reshaping of the EDL in $Zn(SA)_2$ electrolytes (Fig. 4h). 4 M $Zn(SA)_2$ results in a positive shift in the potential of zero charge (PZC, defined as the minimum capacitance) and a lower capacitance. These characteristics verify the design of a dielectric electrochemical interface *via* highly polarizable anions. A recent study presented a comprehensive understanding of SEI formation by sulfamate anions on Zn anodes, based on the hypothesized reduction of preferentially adsorbed SA^-.[19] The stability of the SA^- anion was first studied to examine the details of the electrolyte–Zn interface. The frontier molecular orbitals, *i.e.*, the highest occupied molecular orbital (HOMO) and lowest unoccupied molecular orbital (LUMO) of SA^-, were calculated using DFT (Fig. S20†). Its LUMO was located at 0.52 eV, suggesting that SA^- cannot be easily reduced.[57–59] The reduction stability of SA^- when coupled with metallic Zn was further investigated. The obtained reduction potential of SA^- (−2.94 V *vs.* Zn/Zn^{2+}) is well below that of Zn^0 reduction (Fig. 4h), as evidenced by a symmetric redox pair at 1.18/0.88 V *vs.* Zn/Zn^{2+} uncovered in cyclic voltammetry (CV), which could be ascribed to the adsorption/desorption of SA^- (Fig. S21†).[60–62]

Time-dependent *ex situ* FTIR-ATR and X-ray photoelectron spectroscopy (XPS) were correlated to monitor the SEI growth during subsequent plating/stripping steps. After the first charge, the deposition surface presents broad vibrational features corresponding to NH_3^+ symmetric stretching and degenerate rocking, and $-SO_3^-$ symmetric deformation (Fig. 4i and Table S1†). In the corresponding stripped spectrum, the apparent features of NH_3^+ symmetric stretching, $-NH_2$ stretching, $-SO_3^-$ asymmetric stretching and symmetric deformation, and S=O appear with distinguishable –OH stretching. This is consistent with the surface vibrational characteristics after long-term cycling, namely, $-NH_2$ stretching vibration (~3172 cm^{-1}), NH_3^+ and $-NH_2$ groups (3085–2925 cm^{-1}), symmetric NH_3^+ stretching (2880 cm^{-1}), degenerate NH_3^+ deformation (1559 cm^{-1}), asymmetric $-SO_3^-$ stretching (1301 cm^{-1}) and symmetric $-SO_3^-$ deformation (1038 cm^{-1}), which suggests the presence of SA^- anions on the cycled surface. Accordingly, chemical information was collected for the deposition surface using XPS (Fig. 4j and k). After the first charge, $NH_2SO_3^-$ (170.0 and 168.7 eV, S 2p) and corresponding N–S (397.3 and 399.2 eV, N 1s) peaks are detected, supporting the presence of SA^- during Zn deposition. In parallel, the presence of $-SO_3^-$ (167.8 eV, S 2p) and $-NH_2$ (400.8 eV, N 1s) can be observed in the Zn after the first discharge, and their relative proportions increase from 9.2% to 12.2% and from 24.23% to 37.9% after cycling (at the 100th cycle). Additionally, Zn–OH (Zn 2p) appears on the Zn after the first discharge, and its proportion increases from 33% to 41.4% (Fig. S22 and Table S3†). The XRD spectrum further displays a narrow diffraction peak emerging at ~9.31°, reflecting the crystallinity of the surface structure (Fig. S23†). Consequently, the surface evolution information supports the formation of an SEI on Zn. Considering the electrochemical stability of SA^-, it implies that the structure of the induced SEI could be attributed to the SA^- incorporating zinc hydroxide complex $Zn(SO_3NH_2)_x(OH)_y \cdot nH_2O$.[63] The ionic conductivity of this SEI is estimated to be ~0.26 mS cm^{-1}, which is comparable to those of currently reported novel surface layers for Zn anode.[44,64–69]

V_2O_5/Zn full cell

Further, the influence of anion-derived high-dielectric electrochemical interface on the performance of V_2O_5/Zn full cells was evaluated. Higher activity was observed for the cell with 4 M $Zn(SA)_2$ than its 2 M counterpart or the benchmark 3 M $Zn(OTf)_2$ (Fig. 5a). The cell with 4 M $Zn(SA)_2$ also exhibits lower polarization gaps of ~90 mV (peak l and 2) and ~70 mV (peak 3 and 4) than those for 2 M $Zn(SA)_2$ (~200 mV and ~120 mV) and 3 M $Zn(OTf)_2$ (~120 mV and ~80 mV), suggesting faster reaction kinetics and better reversibility as supported by the stable CV cycling (Fig. S24†). The advantage of 4 M $Zn(SA)_2$ is also supported by the rate performance (Fig. 5b). When the current density increases to 1 A g^{-1}, the cell with 4 M $Zn(SA)_2$ presents a capacity of 370.0 mA h g^{-1}, which is higher than those of 2 M $Zn(SA)_2$ (261.0 mA h g^{-1}) and 3 M $Zn(OTf)_2$ (336.2 mA h g^{-1}). When the current density returns to 0.2 A g^{-1}, the cell with 4 M $Zn(SA)_2$ exhibits a higher capacity retention of 96.6% than its 2 M counterpart (88.0%) and 3 M $Zn(OTf)_2$ (85.6%). The favorable kinetics in the full cell can be attributed to the reduced charge transfer resistance of the electrochemical interface achieved using 4 M $Zn(SA)_2$ (Fig. S25 and Table S4†).

In the galvanostatic charge–discharge (GCD) curve at 0.1 A g^{-1} (Fig. 5c), the cell with 4 M $Zn(SA)_2$ exhibits two distinct sloping discharge/charge regions at ~0.5 and 1.2 V, consistent with the redox peaks in the CV curves (Fig. 5a), giving a capacity of 447.7 mA h g^{-1}. The cycling stability of the V_2O_5/Zn cells was also assessed. At 1 A g^{-1}, the cell with 4 M $Zn(SA)_2$ can retain 88.0% of its maximum capacity after 3000 cycles with nearly 100.0% CE (Fig. S26†). In stark contrast, the cell with 2 M $Zn(SA)_2$ presents only ~20 mA h g^{-1} after 1000 cycles with a poor capacity retention of 5.4%, and that with 3 M $Zn(OTf)_2$ also shows a low retention rate of 29.8% after 2000 cycles. Under a high current density of 10 A g^{-1}, the cell with 4 M $Zn(SA)_2$ delivers superior capacity retention of 89.7% even after 10 000 cycles, compared to 5.3% and 64.2% for 2 M $Zn(SA)_2$ and 3 M $Zn(OTf)_2$ after only 2000 cycles (Fig. 5d). An *ex situ* study was conducted to investigate the change in the V_2O_5 cathode. After long cycling in 4 M $Zn(SA)_2$, the cathode clearly exhibits a diffraction peak at ~7.36° (corresponding to a slightly reduced (001) interlayer spacing of 12.0 Å compared to that of 14.1 Å calculated from the peak at ~6.28° for the pristine state) (Fig. 5e), indicating the good retention of the layered structure of V_2O_5. In contrast, the cathodes in 2 M $Zn(SA)_2$ and 3 M $Zn(OTf)_2$ do not retain their original layered structure, but instead exhibit a phase change to zinc vanadate (ZVO, $Zn_3V_2O_7(OH)_2 \cdot 2H_2O$) (~12.15° for (001)),[71] leading to significant capacity decay. FTIR spectra (Fig. S27 and Table S5†) confirmed that the cathode cycled in 4 M $Zn(SA)_2$ preserves the vibrational characteristics of the VOBV stretching (453 cm^{-1}) and top VOA in-plane stretching (987 cm^{-1}) with reference to the original V_2O_5.[27] Based on the above, the superior cycling stability of

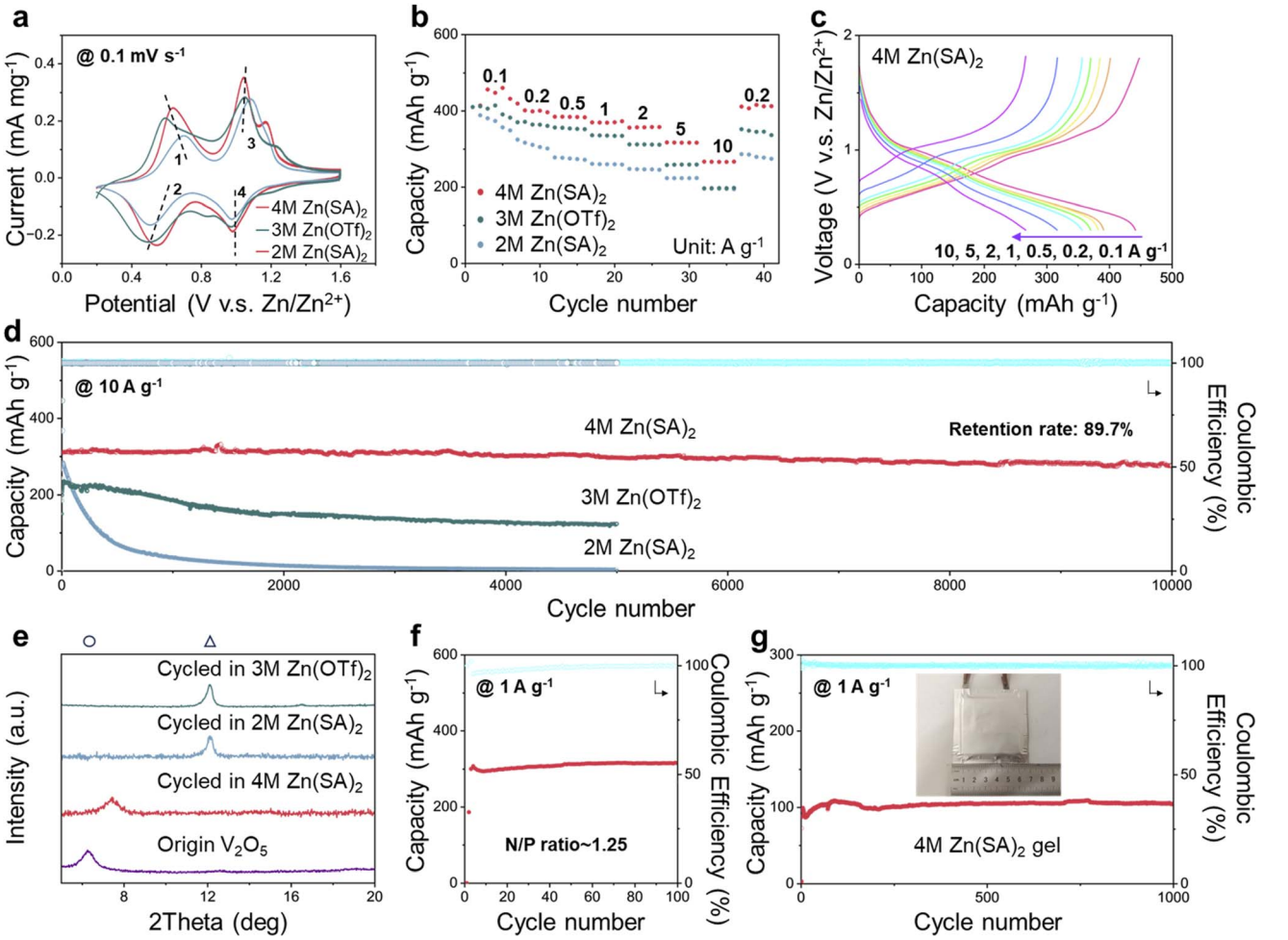

Fig. 5 Performance of ZMB cells. (a) CV curves of the V_2O_5/Zn cells with $Zn(SA)_2$ and $Zn(OTf)_2$ electrolytes at 0.1 mV s^{-1}, in which two redox pairs, *e.g.*, 0.63/0.54 and 1.04/0.97 in 4 M $Zn(SA)_2$, can be attributed to H^+/Zn^{2+} insertion/desertion in mixed valence state V_2O_5.[22,70] (b) Rate performance of the full cells comparing the $Zn(SA)_2$ and $Zn(OTf)_2$ electrolytes. (c) Galvanostatic charge–discharge curves of the cell with 4 M $Zn(SA)_2$ at a series of current densities from 0.1 to 10 A g^{-1}. (d) Long-term cycling of the full cells with zinc aqueous electrolytes at 10 A g^{-1}. (e) *Ex situ* XRD patterns of the cycled V_2O_5 cathodes in different electrolytes at 1 A g^{-1}, which show the presence of crystalline phases of V_2O_5 (○) and ZVO (△). (f) Cycling of the full cell at 1 A g^{-1} with an N/P ratio of ~1.25. (g) Pouch cell with the gel electrolyte cycled at 1 Ag^{-1}.

V_2O_5/Zn with 4 M $Zn(SA)_2$ could be attributed to the following. The electrochemical interface constructed by 4 M $Zn(SA)_2$ favors uniform Zn deposition, promotes exposure of the electrochemically stable Zn (002) facets, and depresses the water activity and surface corrosion. Further, the uniform ion-conducting anion-induced SEI facilitates interfacial reactions compared to its OTf^- counterpart during cycling. It thereby enhances the reversibility of Zn stripping/plating at high CEs. Together with the mildly acidic environment (pH of 4 M $Zn(SA)_2$: ~3.4), it shifts the chemical equilibrium of $V_2O_5 + 3H_2O \leftrightarrow 2VO_2(OH)_2^- + 2H^+$ toward the stabilization of V_2O_5,[71] where an organic-type surface layer formed on V_2O_5 with sulfonate groups (Fig. S27 and S28†) could effectively conduct cations, favoring the interfacial kinetics.[72]

Based on the above merits, a full cell with an N/P ratio of ~1.25 : 1 (*i.e.*, DOD_{Zn} of 80%) was assembled using the Zn deposited by the $Zn(SA)_2$ electrolyte, and showed steady cycling at 1 A g^{-1} with a retention rate of ~100% (Fig. 5f). To further extend the proposed electrochemical interface in ZMBs, 4 M $Zn(SA)_2$@polyacrylamide (PAAm) gel was adopted as an electrolyte *via in situ* polymerization, and greater enhancement of the dielectric properties was observed for the $Zn(SA)_2$@PAAm gel (Fig. 1d). In terms of Zn deposition, the switch to the 3D mode can be further sped up to 152 s (Fig. 3c). The $Zn(SA)_2$@PAAm gel provides a DOD of ~85% at 50 mA cm^{-2} and 50 mA h cm^{-2}, with a lifespan of over 400 h (Fig. S29†). A pouch cell for the gel electrolyte was then fabricated, which showed a promising retention rate of 96.2% at 1 A g^{-1} (Fig. 5g). The scalability and cost effectiveness were further estimated to demonstrate its potential application (Table S6†). The above demonstration verifies the importance of constructing a high-dielectric water-deficient interface for regulating the interface reactions in aqueous rechargeable batteries.

Conclusion

Based on the intercorrelated intrinsic properties of anions for aqueous zinc electrolytes, a high-dielectric water-deficient

electrolyte–Zn interface was constructed using an anion that combines polarizability and H-bond tuning ability; specifically, the representative anion sulfamate was selected. The concentration dependence of the physicochemical properties of $Zn(SA)_2$ aqueous electrolytes was correlated with the solvation structure, which effectively tunes the H-bond characteristics as well as the transport behavior. The SA^- anion-derived interface promotes a fast switch from the 2D to the 3D nucleation mode and achieves uniform Zn deposition with favorable (002) texture formation, whose stability was verified using *in situ* Raman spectroscopy. The constructed electrochemical interface facilitates highly stable Zn stripping/plating, *e.g.*, at 10 mA cm^{-2} and 10 mA h cm^{-2}, and the *in situ* formation of an anion-involved SEI was unveiled based on electrochemically stable SA^- on the interface. Furthermore, the electrochemical interface enables the construction of a V_2O_5/Zn cell with ultra-stable long-term cycling, *e.g.*, 10 000 cycles at 10 A g^{-1}, and its role in stabilizing the V_2O_5 cathode is revealed. The concept of a high-dielectric interface was extended to a gel electrolyte, the use of which achieved high utilization of Zn in a symmetric cell (DOD ~85%) and a promising cycling stability of 96.2% at 1 A g^{-1} in a pouch cell. Hence, the proposed high-dielectric water-deficient interface provides a regulation platform for the promising use of metallic Zn anodes, which also provides guidelines for novel electrolyte design in emerging battery systems.

Data availability

The data supporting this article have been included as part of the ESI.†

Author contributions

X. Liu: conduct experiment, data analysis, draft the manuscript; X. Nie, Y. Yang, J. Zheng: conduct experiment, assist data discussion and analysis; M. Zhou: discussion on salt synthesis; J. Zhao: discussion on interface chemistry; M. Yao, H. Liang: conceptualization, data discussion, revise the manuscript; Y. Chen: calculation, data discussion; D. Yuan: conceptualization, experimental design, data analysis, revise and finalize the manuscript.

Conflicts of interest

There are no conflicts to declare.

Acknowledgements

D. Yuan would like to acknowledge the funding support from the 100 Talented Team of Hunan Province (XiangZu [2016] 91), and the Natural Science Foundation of Hunan Province (2022JJ30613). M. Yao would like to acknowledge the National Natural Science Foundation of China (22408239) and Sichuan Science and Technology Program (2024NSFSC0987). H. Liang would like to acknowledge Fujian Provincial Science and Technology Program for External Cooperation, 2024I0001.

References

1 L. Tang, H. Peng, J. Kang, H. Chen, M. Zhang, Y. Liu, D. H. Kim, Y. Liu and Z. Lin, Zn-based batteries for sustainable energy storage: strategies and mechanisms, *Chem. Soc. Rev.*, 2024, **53**, 4877–4925.
2 Z. Wu, Y. Wang and C. Zhi, Zinc-anode reversibility and capacity inflection as an evaluation criterion, *Joule*, 2024, **8**, 2442–2448.
3 J. Zhu, Z. Tie, S. Bi and Z. Niu, Towards More Sustainable Aqueous Zinc-Ion Batteries, *Angew Chem. Int. Ed. Engl.*, 2024, **63**, e202403712.
4 K. Roy, A. Rana, J. N. Heil, B. M. Tackett and J. E. Dick, For Zinc Metal Batteries, How Many Electrons go to Hydrogen Evolution? An Electrochemical Mass Spectrometry Study, *Angew Chem. Int. Ed. Engl.*, 2024, **63**, e202319010.
5 M. Li, Z. Li, X. Wang, J. Meng, X. Liu, B. Wu, C. Han and L. Mai, Comprehensive understanding of the roles of water molecules in aqueous Zn-ion batteries: from electrolytes to electrode materials, *Energy Environ. Sci.*, 2021, **14**, 3796–3839.
6 J. Wei, P. Zhang, J. Sun, Y. Liu, F. Li, H. Xu, R. Ye, Z. Tie, L. Sun and Z. Jin, Advanced electrolytes for high-performance aqueous zinc-ion batteries, *Chem. Soc. Rev.*, 2024, **53**, 10335–10369.
7 L. Ren, Z. Hu, C. Peng, L. Zhang, N. Wang, F. Wang, Y. Xia, S. Zhang, E. Hu and J. Luo, Suppressing metal corrosion through identification of optimal crystallographic plane for Zn batteries, *Proc. Natl. Acad. Sci. U. S. A.*, 2024, **121**, e2309981121.
8 F. Bu, Z. Sun, W. Zhou, Y. Zhang, Y. Chen, B. Ma, X. Liu, P. Liang, C. Zhong, R. Zhao, H. Li, L. Wang, T. Zhang, B. Wang, Z. Zhao, J. Zhang, W. Li, Y. S. Ibrahim, Y. Hassan, A. Elzatahry, D. Chao and D. Zhao, Reviving Zn0 Dendrites to Electroactive Zn2+ by Mesoporous MXene with Active Edge Sites, *J. Am. Chem. Soc.*, 2023, **145**, 24284–24293.
9 Z. Ju, T. Zheng, B. Zhang and G. Yu, Interfacial chemistry in multivalent aqueous batteries: fundamentals, challenges, and advances, *Chem. Soc. Rev.*, 2024, **53**, 8980–9028.
10 W. Zhong, Z. Shen, J. Mao, S. Zhang, H. Cheng, Y. Kim and Y. Lu, Mitigating cathodic dissolution through interfacial water masking to enhance the longevity of aqueous zinc–ion batteries, *Energy Environ. Sci.*, 2024, **17**, 2059–2068.
11 Y. Liang, M. Qiu, P. Sun and W. Mai, Comprehensive Review of Electrolyte Modification Strategies for Stabilizing Zn Metal Anodes, *Adv. Funct. Mater.*, 2023, **33**, 2304878.
12 G. Gao, X. Huo, B. Li, J. Bi, Z. Zhou, Z. Du, W. Ai and W. Huang, Customizing the water-scarce, zinc ion-rich Helmholtz plane of a zinc anode for Ah-scale Zn metal batteries, *Energy Environ. Sci.*, 2024, **17**, 7850–7859.
13 Y. Pan, Z. Zuo, Y. Jiao and P. Wu, Constructing Lysozyme Protective Layer via Conformational Transition for Aqueous Zn Batteries, *Adv. Mater.*, 2024, **36**, 2314144.
14 S. Chen, Y. Xia, R. Zeng, Z. Luo, X. Wu, X. Hu, J. Lu, E. Gazit, H. Pan, Z. Hong, M. Yan, K. Tao and Y. Jiang, Ordered planar

plating/stripping enables deep cycling zinc metal batteries, *Sci. Adv.*, 2024, **10**, eadn2265.

15 Z. Sun, F. Bu, Y. Zhang, W. Zhou, X. Li, X. Liu, H. Jin, S. Ding, T. Zhang, L. Wang, H. Li, W. Li, C. Zhang, D. Zhao, Y. Wang and D. Chao, Electron-Donating Conjugation Effect Modulated Zn2+ Reduction Reaction for Separator-Free Aqueous Zinc Batteries, *Angew Chem. Int. Ed. Engl.*, 2024, **63**, e202402987.

16 X. Cai, X. Wang, Z. Bie, Z. Jiao, Y. Li, W. Yan, H. J. Fan and W. Song, A Layer-by-Layer Self-Assembled Bio-Macromolecule Film for Stable Zinc Anode, *Adv. Mater.*, 2024, **36**, 2306734.

17 Y. Li, H. Yao, X. Liu, X. Yang and D. Yuan, Roles of electrolyte additive in Zn chemistry, *Nano Res.*, 2023, **16**, 9179–9194.

18 C. Yuan, L. Yin, P. Du, Y. Yu, K. Zhang, X. Ren, X. Zhan and S. Gao, Microgroove-patterned Zn metal anode enables ultra-stable and low-overpotential Zn deposition for long-cycling aqueous batteries, *Chem. Eng. J.*, 2022, **442**, 136231.

19 C. Yuan, J. Xiao, C. Liu and X. Zhan, Elucidating synergistic mechanisms of an anion–cation electrolyte additive for ultra-stable zinc metal anodes, *J. Mater. Chem. A*, 2024, **12**, 19060–19068.

20 H. Yao, Y. Li, Z. Chen, J. Chen, C. F. Du, Y. Chen, J. Chen, M. W. Wong, J. Zhao and D. Yuan, Anion Chemistry towards On-Site Construction of Solid-Electrolyte Interface for Highly Stable Metallic Zn Anode, *Angew Chem. Int. Ed. Engl.*, 2024, **63**, e202411056.

21 J.-L. Yang, L. Liu, Z. Yu, P. Chen, J. Li, P. A. Dananjaya, E. K. Koh, W. S. Lew, K. Liu, P. Yang and H. J. Fan, Dielectric–Metallic Double-Gradient Composition Design for Stable Zn Metal Anodes, *ACS Energy Lett.*, 2023, **8**, 2042–2050.

22 J. Wang, Y. Yu, R. Chen, H. Yang, W. Zhang, Y. Miao, T. Liu, J. Huang and G. He, Induced Anionic Functional Group Orientation-Assisted Stable Electrode-Electrolyte Interphases for Highly Reversible Zinc Anodes, *Adv. Sci.*, 2024, **11**, e2402821.

23 P. Sun, L. Ma, W. Zhou, M. Qiu, Z. Wang, D. Chao and W. Mai, Simultaneous Regulation on Solvation Shell and Electrode Interface for Dendrite-Free Zn Ion Batteries Achieved by a Low-Cost Glucose Additive, *Angew Chem. Int. Ed. Engl.*, 2021, **60**, 18247–18255.

24 N. Zhang, F. Cheng, Y. Liu, Q. Zhao, K. Lei, C. Chen, X. Liu and J. Chen, Cation-Deficient Spinel ZnMn2O4 Cathode in Zn(CF3SO3)2 Electrolyte for Rechargeable Aqueous Zn-Ion Battery, *J. Am. Chem. Soc.*, 2016, **138**, 12894–12901.

25 X. Xu, H. Su, J. Zhang, Y. Zhong, Y. Xu, Z. Qiu, H. B. Wu, X. Wang, C. Gu and J. Tu, Sulfamate-Derived Solid Electrolyte Interphase for Reversible Aqueous Zinc Battery, *ACS Energy Lett.*, 2022, **7**, 4459–4468.

26 S. Chen, D. Ji, Q. Chen, J. Ma, S. Hou and J. Zhang, Coordination modulation of hydrated zinc ions to enhance redox reversibility of zinc batteries, *Nat. Commun.*, 2023, **14**, 3526.

27 D. Yuan, X. Li, H. Yao, Y. Li, X. Zhu, J. Zhao, H. Zhang, Y. Zhang, E. T. J. Jie, Y. Cai and M. Srinivasan, A Liquid Crystal Ionomer-Type Electrolyte toward Ordering-Induced Regulation for Highly Reversible Zinc Ion Battery, *Adv. Sci.*, 2023, **10**, 2206469.

28 H. Du, Y. Dong, Q.-J. Li, R. Zhao, X. Qi, W.-H. Kan, L. Suo, L. Qie, J. Li and Y. Huang, A New Zinc Salt Chemistry for Aqueous Zinc-Metal Batteries, *Adv. Mater.*, 2023, **35**, 2210055.

29 K. Zhou, G. Liu, X. Yu, Z. Li and Y. Wang, Carbonate Ester-Based Electrolyte Enabling Rechargeable Zn Battery to Achieve High Voltage and High Zn Utilization, *J. Am. Chem. Soc.*, 2024, **146**, 9455–9464.

30 J. Xu, H. Li, Y. Jin, D. Zhou, B. Sun, M. Armand and G. Wang, Understanding the Electrical Mechanisms in Aqueous Zinc Metal Batteries: From Electrostatic Interactions to Electric Field Regulation, *Adv. Mater.*, 2024, **36**, 2309726.

31 N. Yao, X. Chen, X. Shen, R. Zhang, Z.-H. Fu, X.-X. Ma, X.-Q. Zhang, B.-Q. Li and Q. Zhang, An Atomic Insight into the Chemical Origin and Variation of the Dielectric Constant in Liquid Electrolytes, *Angew Chem. Int. Ed. Engl.*, 2021, **60**, 21473–21478.

32 S. Zhang, R. Li, T. Deng, Q. Ma, X. Hong, H. Zhang, R. Zhang, S. Ding, Y. Wu, H. Zhu, M. Li, H. Zhang, D. Lu, B. Ma, L. Lv, Y. Li, L. Chen, Y. Shen, R. Guo and X. Fan, Oscillatory solvation chemistry for a 500 Wh kg−1 Li-metal pouch cell, *Nat. Energy*, 2024, **9**, 1285–1296.

33 X. Guo, Z. Ju, X. Qian, Y. Liu, X. Xu and G. Yu, A Stable Solid Polymer Electrolyte for Lithium Metal Battery with Electronically Conductive Fillers, *Angew Chem. Int. Ed. Engl.*, 2023, **62**, e202217538.

34 Y. Zhang, M. Yao, T. Wang, H. Wu and Y. Zhang, A 3D Hierarchical Host with Gradient-Distributed Dielectric Properties toward Dendrite-free Lithium Metal Anode, *Angew Chem. Int. Ed. Engl.*, 2024, **63**, e202403399.

35 D. Xie, Y. Sang, D.-H. Wang, W.-Y. Diao, F.-Y. Tao, C. Liu, J.-W. Wang, H.-Z. Sun, J.-P. Zhang and X.-L. Wu, ZnF2-Riched Inorganic/Organic Hybrid SEI: in situ-Chemical Construction and Performance-Improving Mechanism for Aqueous Zinc-ion Batteries, *Angew Chem. Int. Ed. Engl.*, 2023, **62**, e202216934.

36 Q. Nian, X. Luo, D. Ruan, Y. Li, B.-Q. Xiong, Z. Cui, Z. Wang, Q. Dong, J. Fan, J. Jiang, J. Ma, Z. Ma, D. Wang and X. Ren, Highly reversible zinc metal anode enabled by strong Brønsted acid and hydrophobic interfacial chemistry, *Nat. Commun.*, 2024, **15**, 4303.

37 F. Wang, O. Borodin, T. Gao, X. Fan, W. Sun, F. Han, A. Faraone, J. A. Dura, K. Xu and C. Wang, Highly reversible zinc metal anode for aqueous batteries, *Nat. Mater.*, 2018, **17**, 543–549.

38 H. Yao, Y. Li, Z. Chen, J. Chen, C.-F. Du, Y. Chen, J. Chen, M. W. Wong, J. Zhao and D. Yuan, Anion Chemistry towards On-Site Construction of Solid-Electrolyte Interface for Highly Stable Metallic Zn Anode, *Angew Chem. Int. Ed. Engl.*, 2024, **63**, e202411056.

39 Y. Dong, L. Miao, G. Ma, S. Di, Y. Wang, L. Wang, J. Xu and N. Zhang, Non-concentrated aqueous electrolytes with organic solvent additives for stable zinc batteries, *Chem. Sci.*, 2021, **12**, 5843–5852.

40 Y. Dai, J. Li, C. Zhang, R. Lu, X. Tao, K. A. Owusu, G. He, Y. Zhou and J. Lu, Fluorinated Interphase Enables Reversible Zn2+ Storage in Aqueous ZnSO4 Electrolytes, *ACS Energy Lett.*, 2023, **8**, 4762–4767.
41 X. Zeng, J. Mao, J. Hao, J. Liu, S. Liu, Z. Wang, Y. Wang, S. Zhang, T. Zheng, J. Liu, P. Rao and Z. Guo, Electrolyte Design for In Situ Construction of Highly Zn2+-Conductive Solid Electrolyte Interphase to Enable High-Performance Aqueous Zn-Ion Batteries under Practical Conditions, *Adv. Mater.*, 2021, **33**, 2007416.
42 C. Kittel, *Introduction to Solid State Physics*, John Wiley & Sons, 8th edn, 2004.
43 Q. Zhang, K. Xia, Y. Ma, Y. Lu, L. Li, J. Liang, S. Chou and J. Chen, Chaotropic Anion and Fast-Kinetics Cathode Enabling Low-Temperature Aqueous Zn Batteries, *ACS Energy Lett.*, 2021, **6**, 2704–2712.
44 W. Yuan, G. Ma, X. Nie, Y. Wang, S. Di, L. Wang, J. Wang, S. Shen and N. Zhang, In-situ construction of a hydroxide-based solid electrolyte interphase for robust zinc anodes, *Chem. Eng. J.*, 2022, **431**, 134076.
45 T. Petit, L. Puskar, T. Dolenko, S. Choudhury, E. Ritter, S. Burikov, K. Laptinskiy, Q. Brzustowski, U. Schade, H. Yuzawa, M. Nagasaka, N. Kosugi, M. Kurzyp, A. Venerosy, H. Girard, J.-C. Arnault, E. Osawa, N. Nunn, O. Shenderova and E. F. Aziz, Unusual Water Hydrogen Bond Network around Hydrogenated Nanodiamonds, *J. Phys. Chem. C*, 2017, **121**, 5185–5194.
46 B. Scharifker and G. Hills, Theoretical and experimental studies of multiple nucleation, *Electrochim. Acta*, 1983, **28**, 879–889.
47 R. Zhao, H. Wang, H. Du, Y. Yang, Z. Gao, L. Qie and Y. Huang, Lanthanum nitrate as aqueous electrolyte additive for favourable zinc metal electrodeposition, *Nat. Commun.*, 2022, **13**, 3252.
48 L. Benea and E. Danaila, Nucleation and Growth Mechanism of Ni/TiO2 Nanoparticles Electro-Codeposition, *J. Electrochem. Soc.*, 2016, **163**, D655.
49 S. Zhang, R. Li, T. Deng, Q. Ma, X. Hong, H. Zhang, R. Zhang, S. Ding, Y. Wu, H. Zhu, M. Li, H. Zhang, D. Lu, B. Ma, L. Lv, Y. Li, L. Chen, Y. Shen, R. Guo and X. Fan, Oscillatory solvation chemistry for a 500 Wh kg−1 Li-metal pouch cell, *Nat. Energy*, 2024, **9**, 1285–1296.
50 Z. Ju, T. Zheng, B. Zhang and G. Yu, Interfacial chemistry in multivalent aqueous batteries: fundamentals, challenges, and advances, *Chem. Soc. Rev.*, 2024, **53**, 8980–9028.
51 Z. Chen, Y. Wang, Q. Wu, C. Wang, Q. He, T. Hu, X. Han, J. Chen, Y. Zhang, J. Chen, L. Yang, X. Wang, Y. Ma and J. Zhao, Grain Boundary Filling Empowers (002)-Textured Zn Metal Anodes with Superior Stability, *Adv. Mater.*, 2024, 2411004.
52 Z. Chen, Q. Wu, X. Han, C. Wang, J. Chen, T. Hu, Q. He, X. Zhu, D. Yuan, J. Chen, Y. Zhang, L. Yang, Y. Ma and J. Zhao, Converting Commercial Zn Foils into Single (002)-Textured Zn with Millimeter-Sized Grains for Highly Reversible Aqueous Zinc Batteries, *Angew Chem. Int. Ed. Engl.*, 2024, **63**, e202401507.
53 J. Zhang, W. Huang, L. Li, C. Chang, K. Yang, L. Gao and X. Pu, Nonepitaxial Electrodeposition of (002)-Textured Zn Anode on Textureless Substrates for Dendrite-Free and Hydrogen Evolution-Suppressed Zn Batteries, *Adv. Mater.*, 2023, **35**, 2300073.
54 Z. Hao, Y. Zhang, Z. Hao, G. Li, Y. Lu, S. Jin, G. Yang, S. Zhang, Z. Yan, Q. Zhao and J. Chen, Metal Anodes with Ultrahigh Reversibility Enabled by the Closest Packing Crystallography for Sustainable Batteries, *Adv. Mater.*, 2023, **35**, 2209985.
55 D. Yuan, J. Zhao, H. Ren, Y. Chen, R. Chua, E. T. J. Jie, Y. Cai, E. Edison, W. Manalastas Jr, M. W. Wong and M. Srinivasan, Anion Texturing Towards Dendrite-Free Zn Anode for Aqueous Rechargeable Batteries, *Angew Chem. Int. Ed. Engl.*, 2021, **60**, 7213–7219.
56 J. Zheng, Q. Zhao, T. Tang, J. Yin, C. D. Quilty, G. D. Renderos, X. Liu, Y. Deng, L. Wang, D. C. Bock, C. Jaye, D. Zhang, E. S. Takeuchi, K. J. Takeuchi, A. C. Marschilok and L. A. Archer, Reversible epitaxial electrodeposition of metals in battery anodes, *Science*, 2019, **366**, 645–648.
57 X.-B. Cheng, R. Zhang, C.-Z. Zhao and Q. Zhang, Toward Safe Lithium Metal Anode in Rechargeable Batteries: A Review, *Chem. Rev.*, 2017, **117**, 10403–10473.
58 P. Peljo and H. H. Girault, Electrochemical potential window of battery electrolytes: the HOMO–LUMO misconception, *Energy Environ. Sci.*, 2018, **11**, 2306–2309.
59 J. Lopez, D. G. Mackanic, Y. Cui and Z. Bao, Designing polymers for advanced battery chemistries, *Nat. Rev. Mater.*, 2019, **4**, 312–330.
60 C. Yan, H.-R. Li, X. Chen, X.-Q. Zhang, X.-B. Cheng, R. Xu, J.-Q. Huang and Q. Zhang, Regulating the Inner Helmholtz Plane for Stable Solid Electrolyte Interphase on Lithium Metal Anodes, *J. Am. Chem. Soc.*, 2019, **141**, 9422–9429.
61 X. Wang, M. Salari, D.-E. Jiang, J. Chapman Varela, B. Anasori, D. J. Wesolowski, S. Dai, M. W. Grinstaff and Y. Gogotsi, Electrode material–ionic liquid coupling for electrochemical energy storage, *Nat. Rev. Mater.*, 2020, **5**, 787–808.
62 R. Subbaraman, D. Strmcnik, V. Stamenkovic and N. M. Markovic, Three Phase Interfaces at Electrified Metal−Solid Electrolyte Systems 1. Study of the Pt(hkl)−Nafion Interface, *J. Phys. Chem. C*, 2010, **114**, 8414–8422.
63 N. V. Zubkova, I. V. Pekov, N. V. Chukanov, D. A. Ksenofontov, V. O. Yapaskurt, S. N. Britvin and D. Y. Pushcharovsky, A New Sulfamate Cu3(OH)5 [SO3(NH2)]: A Product of the Anthropogenic Alteration of Copper Sulfides, *Moscow Univ. Geol. Bull.*, 2022, **77**, 617–622.
64 X. Guo, J. Lu, M. Wang, A. Chen, H. Hong, Q. Li, J. Zhu, Y. Wang, S. Yang, Z. Huang, Y. Wang, Z. Pei and C. Zhi, Solid-electrolyte interphase governs zinc ion transfer kinetics in high-rate and stable zinc metal batteries, *Chem*, 2024, **10**, 3607–3612.
65 P. Xiong, Y. Kang, N. Yao, X. Chen, H. Mao, W.-S. Jang, D. M. Halat, Z.-H. Fu, M.-H. Jung, H. Y. Jeong, Y.-M. Kim, J. A. Reimer, Q. Zhang and H. S. Park, Zn-Ion

Transporting, In Situ Formed Robust Solid Electrolyte Interphase for Stable Zinc Metal Anodes over a Wide Temperature Range, *ACS Energy Lett.*, 2023, **8**, 1613–1625.

66 Y. Zhou, G. Li, S. Feng, H. Qin, Q. Wang, F. Shen, P. Liu, Y. Huang and H. He, Regulating Zn Ion Desolvation and Deposition Chemistry Toward Durable and Fast Rechargeable Zn Metal Batteries, *Adv. Sci.*, 2023, **10**, 2205874.

67 D. Han, C. Cui, K. Zhang, Z. Wang, J. Gao, Y. Guo, Z. Zhang, S. Wu, L. Yin, Z. Weng, F. Kang and Q.-H. Yang, A non-flammable hydrous organic electrolyte for sustainable zinc batteries, *Nat. Sustainability*, 2021, **5**, 205–213.

68 M. Yao, R. Pan, Y. Ren, Y. Fu, Y. Qin, C. Mao, Z. Zhang, X. Guo and G. Li, Regulating solvation shells and interfacial chemistry in zinc-ion batteries using glutaronitrile based electrolyte, *J. Mater. Chem. A*, 2022, **10**, 14345–14354.

69 J. Hao, B. Li, X. Li, X. Zeng, S. Zhang, F. Yang, S. Liu, D. Li, C. Wu and Z. Guo, An In-Depth Study of Zn Metal Surface Chemistry for Advanced Aqueous Zn-Ion Batteries, *Adv. Mater.*, 2020, **32**, e2003021.

70 J. Zhao, H. Ren, Q. Liang, D. Yuan, S. Xi, C. Wu, W. Manalastas, J. Ma, W. Fang, Y. Zheng, C.-F. Du, M. Srinivasan and Q. Yan, High-performance flexible quasi-solid-state zinc-ion batteries with layer-expanded vanadium oxide cathode and zinc/stainless steel mesh composite anode, *Nano Energy*, 2019, **62**, 94–102.

71 Y. Kim, Y. Park, M. Kim, J. Lee, K. J. Kim and J. W. Choi, Corrosion as the origin of limited lifetime of vanadium oxide-based aqueous zinc ion batteries, *Nat. Commun.*, 2022, **13**, 2371.

72 Y. Dai, C. Zhang, J. Li, X. Gao, P. Hu, C. Ye, H. He, J. Zhu, W. Zhang, R. Chen, W. Zong, F. Guo, I. P. Parkin, D. J. L. Brett, P. R. Shearing, L. Mai and G. He, Inhibition of Vanadium Cathodes Dissolution in Aqueous Zn-Ion Batteries, *Adv. Mater.*, 2024, **36**, 2310645.